

REST-FRAME OPTICAL SPECTRA OF THREE STRONGLY LENSED GALAXIES AT $Z \sim 2$ ¹

KEVIN N. HAINLINE, ALICE E. SHAPLEY^{2,3}, AND KATHERINE A. KORNEI

Department of Astronomy, University of California, Los Angeles, 430 Portola Plaza, Los Angeles, CA 90024

MAX PETTINI

Institute of Astronomy, University of Cambridge, Madingley Road, Cambridge CB3 0HA, UK

AND

ELIZABETH BUCKLEY-GEER, SAHAR S. ALLAM, AND DOUGLAS L. TUCKER

Fermi National Accelerator Laboratory, Batavia, IL 60510

Received DATE; accepted DATE

ABSTRACT

We present Keck II NIRSPEC rest-frame optical spectra for three recently discovered lensed galaxies: the Cosmic Horseshoe ($z = 2.38$), the Clone ($z = 2.00$), and SDSS J090122.37+181432.3 ($z = 2.26$). The boost in signal-to-noise ratio (S/N) from gravitational lensing provides an unusually detailed view of the physical conditions in these objects. A full complement of high S/N rest-frame optical emission lines is measured, spanning from rest-frame 3600 to 6800 Å, including robust detections of fainter lines such as H γ , [S II] λ 6717,6732, and in one instance [Ne III] λ 3869. SDSS J090122.37+181432.3 shows evidence for AGN activity, and therefore we focus our analysis on star-forming regions in the Cosmic Horseshoe and the Clone. For these two objects, we estimate a wide range of physical properties. Current lensing models for the Cosmic Horseshoe and the Clone allow us to correct the measured H α luminosity and calculated star-formation rate (SFR). Metallicities have been estimated with a variety of indicators, which span a range of values of $12 + \log(\text{O}/\text{H}) = 8.3 - 8.8$, between ~ 0.4 and ~ 1.5 of the solar oxygen abundance. Dynamical masses were computed from the H α velocity dispersions and measured half-light radii of the reconstructed sources. A comparison of the Balmer lines enabled measurement of dust reddening coefficients. Variations in the line ratios between the different lensed images are also observed, indicating that the spectra are probing different regions of the lensed galaxies. In all respects, the lensed objects appear fairly typical of UV-selected star-forming galaxies at $z \sim 2$. The Clone occupies a position on the emission-line diagnostic diagram of [O III]/H β vs. [N II]/H α that is offset from the locations of $z \sim 0$ galaxies. Our new NIRSPEC measurements may provide quantitative insights into why high-redshift objects display such properties. From the [S II] line ratio, high electron densities ($\sim 1000 \text{ cm}^{-3}$) are inferred compared to local galaxies, and [O III]/[O II] line ratios indicate higher ionization parameters compared to the local population. Building on previous similar results at $z \sim 2$, these measurements provide further evidence (at high S/N) that star-forming regions are significantly different in high-redshift galaxies, compared to their local counterparts.

Subject headings: gravitational lensing — galaxies: abundances — galaxies: evolution — galaxies: high-redshift

1. INTRODUCTION

A wealth of information about star-forming galaxies is contained in their optical spectra. The ratios of the fluxes of optical emission lines can be used to understand the physical conditions of the gas and stars in star-forming regions, including metallicities, temperatures, densities, and ionization parameters. Near-infrared spectroscopy is used to study these properties in high-redshift galaxies, as the strong rest-frame optical lines are redshifted into the near-IR at $z > 1.5$. These lines include [O II] λ 3727, H β , [O III] λ 5007,4959, H α , [N II] λ 6584,

and [S II] λ 6717,6731, and can be used to infer the oxygen abundance, electron density and ionization parameter in H II regions.

Results from a small existing sample indicate that $z \sim 2$ galaxies have intrinsically different rest-frame optical line ratios from those in the bulk of nearby H II regions and Sloan Digital Sky Survey (SDSS) star-forming galaxies (Erb et al. 2006a; Shapley et al. 2005; Liu et al. 2008). This difference appears in the emission-line diagnostic diagram of [O III]/H β vs. [N II]/H α , where high-redshift star-forming regions are found offset from an extremely tight sequence formed by local objects (Kauffmann et al. 2003). The offset may be caused by differences in the SFR, average ionization parameter, shape of the stellar ionizing spectrum, H II electron density, or the increased contribution of an AGN or shocked gas to the integrated spectra. Based on the analysis of SDSS local star-forming galaxies, Brinchmann et al.

¹ Based, in part, on data obtained at the W.M. Keck Observatory, which is operated as a scientific partnership among the California Institute of Technology, the University of California, and NASA, and was made possible by the generous financial support of the W.M. Keck Foundation.

² Alfred P. Sloan Fellow

³ David and Lucile Packard Fellow

(2008) suggest that an elevated ionization parameter due to high electron densities and non-zero escape fractions of hydrogen ionizing photons is the primary factor. Specifying the cause of this offset using direct measurements from high-redshift galaxies will provide new insight into the physical conditions and chemical abundances of the gas in which the stars were being formed during the epoch when the star-formation activity of the Universe was at its peak (Madau et al. 1996; Steidel et al. 1999; Bouwens et al. 2007).

The optimal redshift range for this type of analysis using ground-based near-IR spectroscopy is $z = 2.0 - 2.5$. In this range, the largest number of strong and weak nebular emission lines falls within the windows of atmospheric transmission and bluewards of the bright thermal IR background at $\lambda \geq 2.35\mu\text{m}$. However, $z \sim 2$ UV-selected galaxies typically have faint magnitudes ($K_{Vega} > 20.0$ mag) and small angular sizes ($\leq 1''$). Thus, it is difficult to obtain the high S/N spectra that are necessary for a truly detailed view of high-redshift star-forming regions using anything but long integration times with the largest telescope apertures. This problem can be addressed by taking advantage of the boost provided by gravitational lensing, which magnifies and offers more sensitive views of distant galaxies.

The best-studied high-redshift lensed galaxy is MS 1512-cB58 ($z = 2.73$, Yee et al. 1996), a typical $\sim L^*$ Lyman break galaxy (LBG). The high magnification (~ 30 , Williams & Lewis 1996; Seitz et al. 1998) of cB58 has allowed for unusually sensitive analyses of the galaxy's rest-frame UV (Pettini et al. 2000, 2002), optical (Teplitz et al. 2000), IR (Siana et al. 2008), and far-IR (Sawicki 2001; Baker et al. 2001) spectra and photometry. In particular, rest-frame optical spectra were used to calculate dust extinction, virial mass, chemical abundances, and SFRs. Recently, new search techniques for strongly-lensed high-redshift galaxies have yielded additional candidates which have been spectroscopically confirmed to lie at $z > 2$ (Allam et al. 2007; Smail et al. 2007). Three of these candidates, SDSS J090122.37+181432.3 ($z = 2.26$, hereafter referred to as SDSS J0901+1814; Diehl et al. 2009, in preparation), the Cosmic Horseshoe ($z = 2.38$; Belokurov et al. 2007), and the Clone ($z = 2.00$; Lin et al. 2008) are at redshifts even better-suited to rest-frame optical spectroscopy than cB58. Analysis of the rest-frame optical spectra of these objects presents a unique opportunity to study both H II region physics and the difference between local star-forming galaxies and those at high-redshift.

In this paper, we analyze Keck II NIRSPEC spectra for these three lensed objects. In §2 we describe the observations, data reduction, and line flux measurements. We discuss several physical quantities derived from these line fluxes in §3. We investigate how our objects compare to other objects at $z \sim 2$ in §4, and review the physical quantities for these objects in order to explain the differences in the physical conditions between high-redshift and local H II regions. Finally, we conclude in §5. Throughout, we assume a cosmology with $\Omega_M = 0.27$, $\Omega_\Lambda = 0.73$, and $H_0 = 71 \text{ km s}^{-1} \text{ Mpc}^{-1}$.

2. OBSERVATIONS AND DATA REDUCTION

2.1. NIRSPEC Observations

We obtained near-IR spectra on 2008 February 19 using the NIRSPEC spectrograph (McLean et al. 1998) on the Keck II telescope. Our targets included three strongly lensed high redshift galaxies: SDSS J090122.37, the Cosmic Horseshoe, and the Clone (Diehl et al. 2009; Belokurov et al. 2007; Lin et al. 2008). At $z \sim 2$, several strong rest-frame optical lines fall within windows of atmospheric transmission in the near-IR. H α and [N II] fall within the NIRSPEC 6 (similar to K -band) filter for all three objects. H γ , [O III] λ 4363, H β , and [O III] λ 4959,5007 fall in the NIRSPEC 5 (similar to H -band) filter for the Cosmic Horseshoe and SDSS J090122.37, and NIRSPEC 4 for the Clone. [O II] and [Ne III] fall in the NIRSPEC 3 (similar to J -band) filter for the Cosmic Horseshoe and SDSS J090122.37, and NIRSPEC 2 for the Clone. Exposure times for the different filters ranged from 3×600 s to 9×600 s, and are listed in Table 1. All targets were observed with a $0''.76 \times 42''$ long slit. Conditions were photometric during the night and seeing ranged from $0''.4 - 0''.9$. The spectral resolution as determined from sky lines was $\sim 10 \text{ \AA}$ for the NIRSPEC-2, -3, -4, and -5 filters, and $\sim 15 \text{ \AA}$ for the NIRSPEC-6 filter. For each object, we placed the slit across two of the lensed images to look for variation in the line ratios between them. The slit position angles (in degrees east of north) were 7.22° for SDSS J090122.37, 10.73° for the Cosmic Horseshoe, and 219.97° for the Clone, and were determined by the locations of high surface brightness knots in the optical lensed images. The separation between the different apertures are $12''.52$ for SDSS J090122.37, $8''.82$ for the Cosmic Horseshoe, and $3''.95$ for the Clone. Images of the objects with slits overlaid are presented in Figure 1.

2.2. Data Reduction and Optimal Background Subtraction

Data reduction was performed following the procedure described in Liu et al. (2008), where the sky background was subtracted using an optimal method on the two-dimensional spectral images (Kelson 2003, Becker, private communication). One notable exception to this procedure addressed the matter of pattern noise. A large fraction of the exposures taken in 2008 February were affected by pattern noise, which consisted of a constant positive or negative offset in the mean count level in every 8th row of the upper-right hand quadrant of the NIRSPEC CCD images. Prior to the standard reduction procedure, we removed this pattern noise in all 75 of the science images.

Sky subtraction for the Cosmic Horseshoe observations required extra care, due to the presence of continuum emission in the slit from the outskirts of the lensing galaxy (a luminous red galaxy at $z = 0.444$; Belokurov et al. 2007). Indeed, the first stage of sky subtraction typically consisted of a simple difference of adjacent, dithered exposures. The dithers adopted for this target were (unfortunately) similar in size to the spacing between the positions of the Horseshoe and lens images, leading to the subtraction of the lens continuum (rather than blank sky) from the Horseshoe in some pairs of exposures. We quantified and corrected for this effect using pairs of exposures in which no oversubtraction occurred.

One-dimensional spectra were extracted from these two-dimensional reduced images along with error spec-

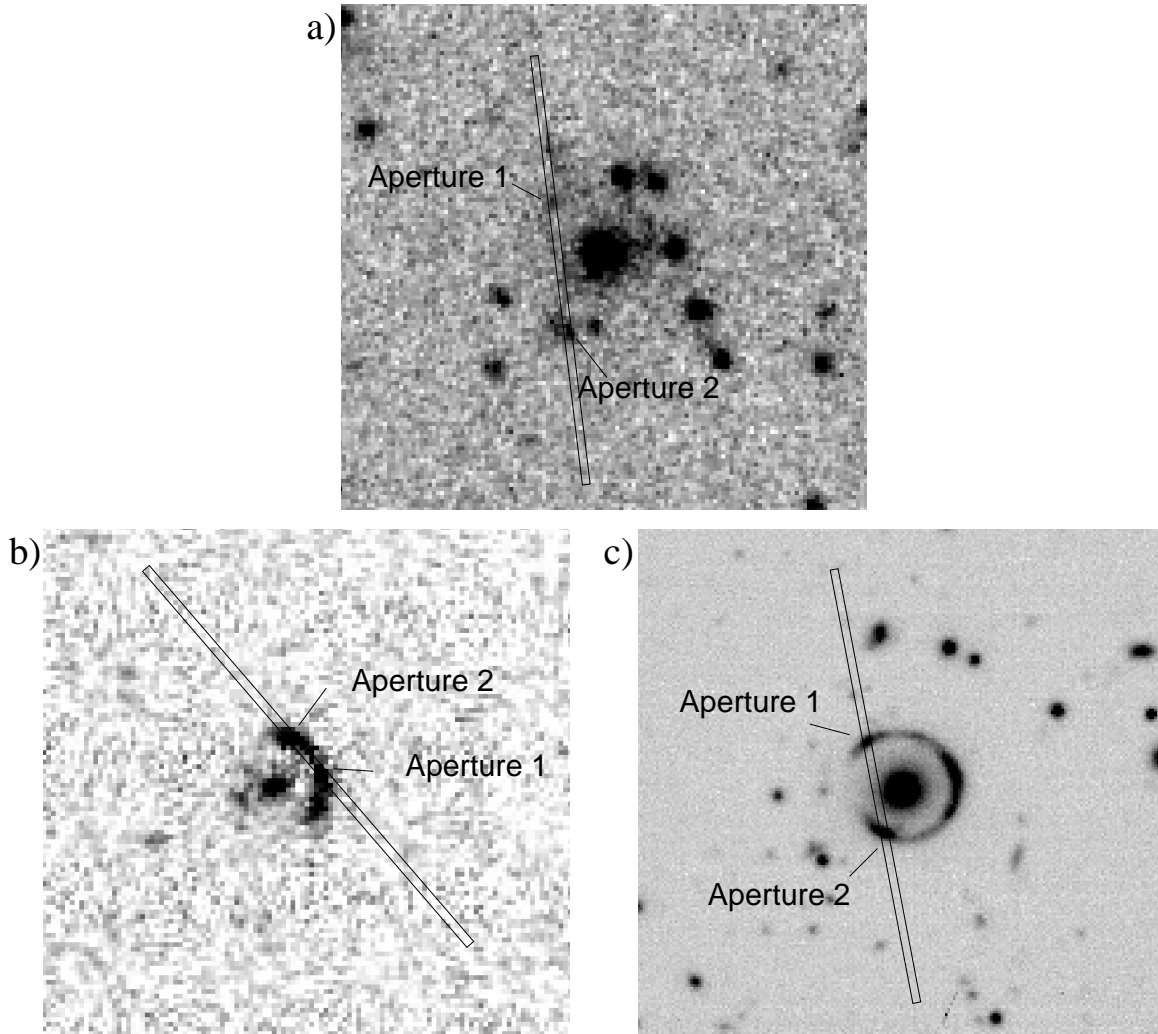


FIG. 1.— Images of the Objects with the NIRSPEC slit overlaid, defining the various apertures used in the paper. a) SDSS J0901+1814, from a SDSS r -band image, b) The Clone, from a SDSS g -band image, and c) The Cosmic Horseshoe, from a VLT/FORS2 R -band image (Lindsay King, private communication). The NIRSPEC slit shown is $0''.76 \times 42''$, and the separation between the different apertures are $12''.52$ for SDSS J0901+1814, $3''.95$ for the Clone., and $8''.82$ for the Cosmic Horseshoe.

TABLE 1
GALAXIES OBSERVED WITH KECK II NIRSPEC

NAME	R.A. (J2000)	Dec. (J2000)	$z_{H\alpha}$	$r(mag)$	$g - r(mag)^a$	Exposure (s)	Band
SDSS J0901+1814	09 01 22.37	18 14 32.35	2.2586	20.6	0.52, 0.21	3×600	J
						6×600	H
						6×600	K
Cosmic Horseshoe	11 48 33.14	19 30 3.20	2.3813	19.0	0.29, 0.25	3×600	J
						9×600	H
						8×600	K
Clone	12 06 2.09	51 42 29.52	2.0026	19.0	0.39, 0.30, 0.34	3×600	J
						3×600	H
						3×600	K

NOTE. — Units of right ascension are hours, minutes, and seconds, and units of declination are degrees, arcminutes and arcseconds.
^a These colors are listed for apertures 1, 2, and in the case of the Clone, the full aperture as shown in Figure 1.

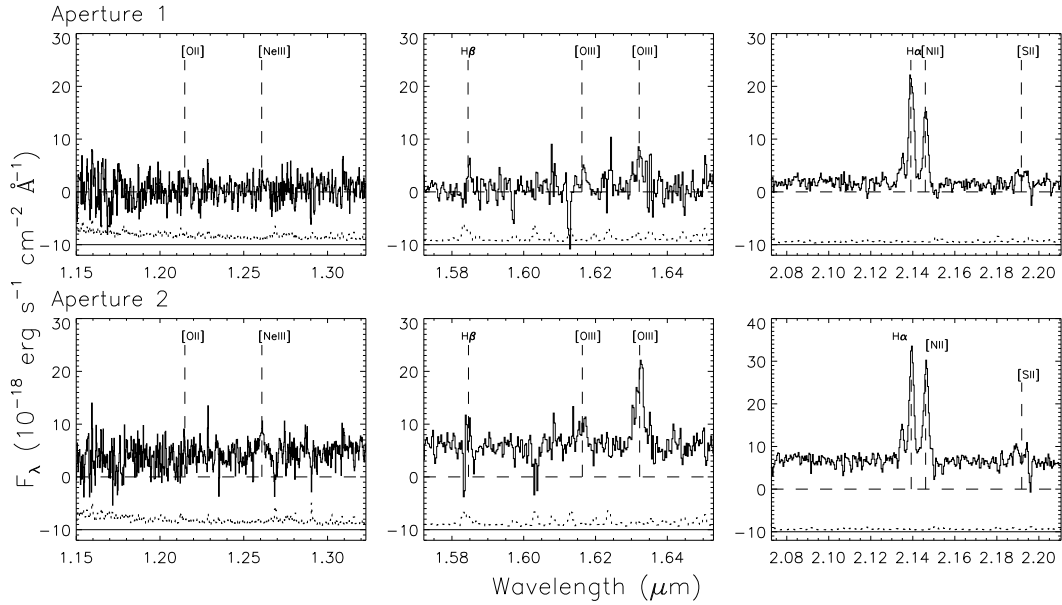


FIG. 2.— NIRSPEC spectrum of SDSS J0901+1814. The top row contains the J , H , and K -band spectra for aperture 1, while the bottom row shows those for aperture 2. Apertures 1 and 2 are as labelled in Figure 1. The positions of the prominent emission lines are indicated. The dotted lower spectrum indicates the 1σ errors offset vertically by $-10 \times 10^{-18} \text{ erg s}^{-1} \text{ cm}^{-2} \text{ \AA}^{-1}$ for clarity. Larger errors occur at the position of the sky lines and at points of high atmospheric extinction.

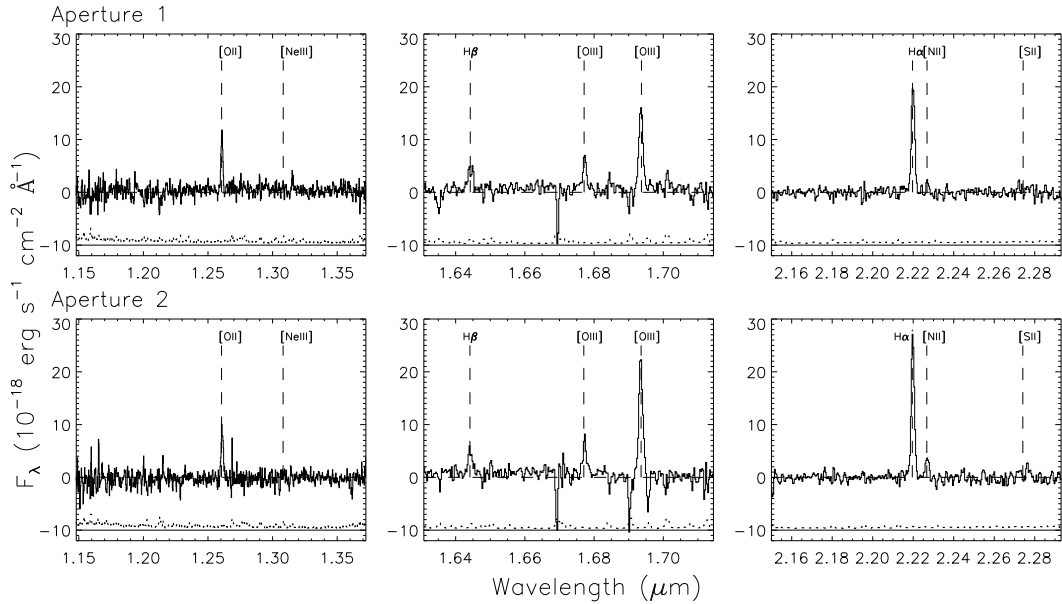


FIG. 3.— NIRSPEC spectrum of the Cosmic Horseshoe. The top row contains the J , H , and K -band spectra for aperture 1, while the bottom row shows those for aperture 2. Apertures 1 and 2 are as labelled in Figure 1. The positions of the prominent emission lines are indicated. The dotted lower spectrum indicates the 1σ errors offset vertically by $-10 \times 10^{-18} \text{ erg s}^{-1} \text{ cm}^{-2} \text{ \AA}^{-1}$ for clarity. Larger errors occur at the position of the sky lines and at points of high atmospheric extinction.

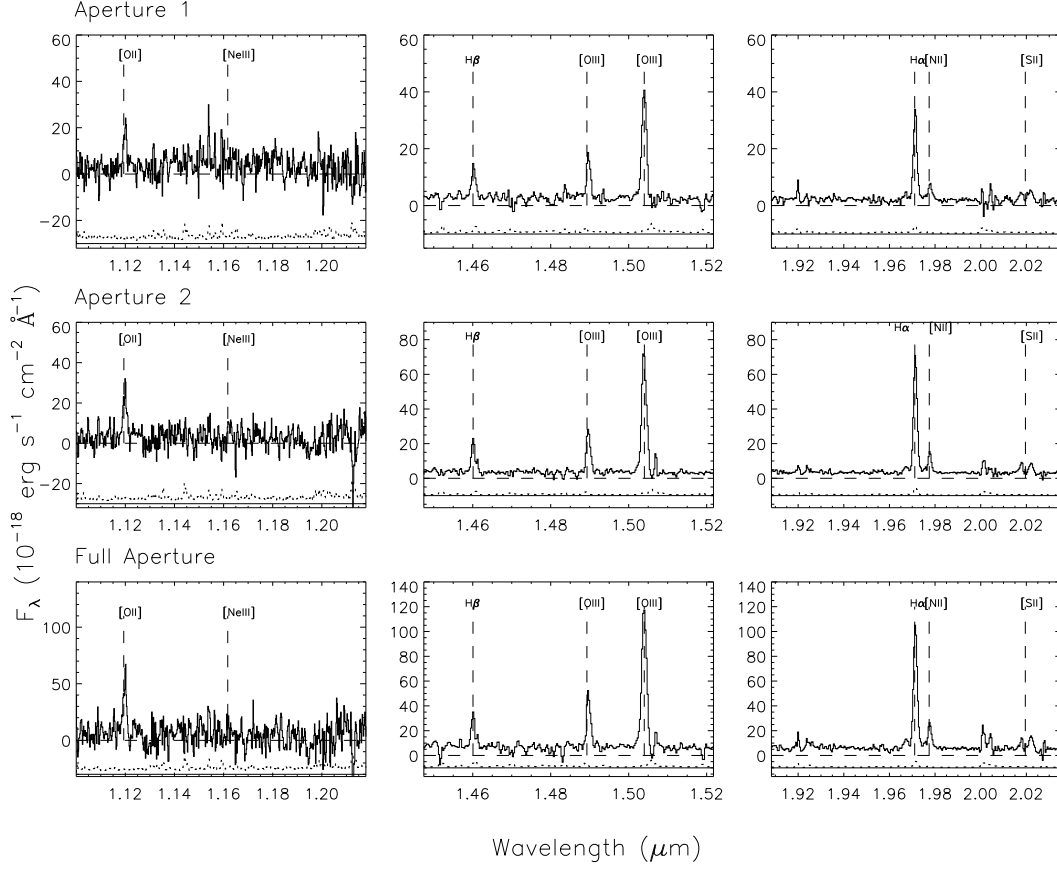


FIG. 4.— NIRSPEC spectrum of the Clone. The top row contains the J , H , and K -band spectra for aperture 1, the second row shows those for aperture 2, and the bottom row shows those from the full aperture. Apertures 1 and 2 are as labelled in Figure 1. The positions of the prominent emission lines are indicated. The dotted lower spectrum indicates the 1σ errors offset vertically by $-30 \times 10^{-18} \text{ erg s}^{-1} \text{ cm}^{-2} \text{ \AA}^{-1}$ for the J -band spectra, and $-10 \times 10^{-18} \text{ erg s}^{-1} \text{ cm}^{-2} \text{ \AA}^{-1}$ for the H - and K -band spectra for clarity. Larger errors occur at the position of the sky lines and at points of high atmospheric extinction.

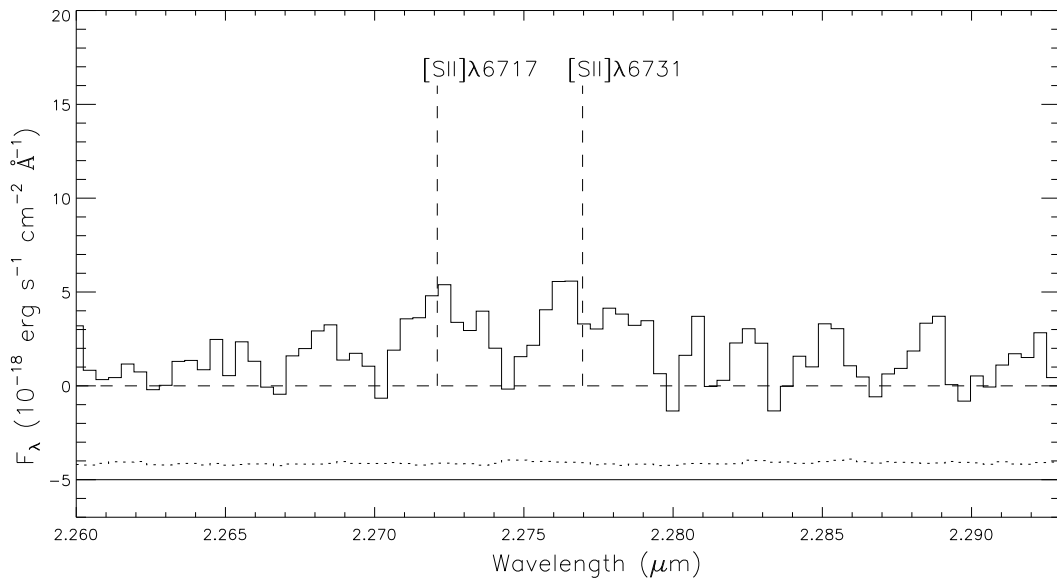


FIG. 5.— NIRSPEC summed spectra from both Cosmic Horseshoe apertures, for the [SII] doublet. The dotted lower spectrum indicates the 1σ errors offset vertically by $-5 \times 10^{-18} \text{ erg s}^{-1} \text{ cm}^{-2} \text{ \AA}^{-1}$ for clarity.

tra. For all three of our objects we extracted apertures for each of the two lensed images covered. For the Clone, the lensed objects almost overlapped, so we extracted a third, full aperture that extended along the slit across both lensed images. These spectra were then flux-calibrated using A-type star observations according to the method described in Shapley et al. (2005) and Erb et al. (2003).

2.3. Line Flux Measurements

One-dimensional, flux-calibrated spectra are shown along with the error spectra in Figures 2, 3, and 4. The error spectrum represents the 1σ uncertainty in the flux at each wavelength. In addition, zoomed-in regions of select portions of the spectra are featured in Figures 5 and 6. The redshifts of the lensed objects were measured by fitting a Gaussian profile to the $H\alpha$ emission feature. In all cases, the redshifts from the separate components of the lensed image pairs agreed to within $\Delta z/(1+z) = 0.0001$ ($\Delta v = 27 - 30 \text{ km s}^{-1}$).

The lines that we set out to measure were [O II] $\lambda\lambda 3726, 3729$, [Ne III] $\lambda 3869$, $H\gamma$, [O III] $\lambda 4363$, $H\beta$, [O III] $\lambda\lambda 4959, 5007$, $H\alpha$, [N II] $\lambda 6584$, and [S II] $\lambda\lambda 6717, 6732$. Line fluxes were determined by fitting Gaussian profiles using the IRAF task, SPLOT. The $H\beta$, $H\gamma$, and [O II] $\lambda\lambda 3726, 3729$ lines were measured individually, while the pairs of [O III] $\lambda\lambda 4959, 5007$, $H\alpha$ and [N II] $\lambda 6584$, and [S II] $\lambda\lambda 6717, 6732$ were fitted simultaneously. With this method, we fixed the central wavelength and FWHM based on the best-fit parameters for the brighter line and then obtained a combined fit for the relative fluxes of the two lines.

In some cases, we had to measure specific lines through different methods because of the presence of sky lines, or the weak fluxes of the lines. For the Cosmic Horseshoe and, to a lesser extent, the Clone, sky systematics were an issue. In both objects, the $H\beta$ line was detected, but its wavelength coincided with that of a strong sky line. Accordingly, we treated the measured $H\beta$ line flux as a lower limit. In §3, we describe a method for recovering the actual $H\beta$ flux in the face of sky systematics. We measured a lower limit on the line flux for the $H\beta$ and [S II] $\lambda 6732$ features of aperture 2 of SDSS J0901+1814 as these lines were over-subtracted on one side during the sky subtraction process. We placed upper limits on the [O III] $\lambda 4363$ line fluxes in all apertures, and on the [Ne III] $\lambda 3869$ line fluxes in all but aperture 1 of SDSS J0901+1814 where it was detected. We summed the flux across both of the [S II] lines for aperture 1 of both SDSS J0901+1814 and the Cosmic Horseshoe due to the low flux from the individual lines.

Uncertainties in line fluxes were estimated using a Monte Carlo approach. For each aperture and filter, we generated five hundred artificial spectra. Fake spectra were created by perturbing the flux at each wavelength of the true spectrum by a random amount consistent with the 1σ error spectrum. Line fluxes were measured from these simulated spectra using the same procedure that was applied to the actual data. The standard deviation of the distribution of line fluxes measured from the artificial spectra was adopted as the error on each line flux measurement. Emission-line fluxes and associated uncertainties are given in Table 2.

3. PHYSICAL QUANTITIES

The flux measurement of rest-frame optical emission lines allows us to probe the physical state of the interstellar gas in the target objects. Because of the magnification provided by gravitational lensing, we have detected lines with a higher signal-to-noise ratio (S/N) than what is typically seen in unlensed high-redshift objects. We can measure dust extinction from the ratios of the Balmer lines of $H\alpha$, $H\beta$, and $H\gamma$, while the $H\alpha$ line offers the highest S/N measure of the gas velocity dispersion, as well as the SFR of the galaxy. The set of [O III] $\lambda\lambda 4959, 5007$, [O II] $\lambda\lambda 3726, 3729$, [N II] $\lambda 6584$ and Balmer emission lines provides multiple methods of determining the gas-phase oxygen abundance. The ratio of [O II] and [O III] lines offers a probe of the ionization parameter of the star-forming regions. Finally, we can use our detection of the [S II] $\lambda\lambda 6717, 6732$ lines and an upper limit of the [O III] $\lambda 4363$ line to estimate the electron density and electron temperature of the gas. Table 3 lists several relevant line ratios and the physical quantities derived from them, as described in the sections below.

3.1. AGN Contamination

We measured the ratio of [N II]/ $H\alpha = 0.65 \pm 0.03$ and 0.88 ± 0.03 for the two apertures of SDSS J0901+1814. Such high ratios, especially in the second aperture, cannot be produced in star-forming regions from photoionization by massive stars (Kewley et al. 2001a; Kauffmann et al. 2003). We therefore infer the presence of an AGN. With insights from the lens model for this system, the AGN can be probed on smaller scales than is typically possible at $z \sim 2$. Such analysis, however, is outside the scope of the current work. For our study of the majority of physical quantities, we focus on the Cosmic Horseshoe and the Clone, where the line fluxes do not appear to be contaminated by the presence of an AGN.

3.2. Velocity Dispersion

The velocity dispersion is a measure of the dynamics of the gas bound to the galaxy by gravity. We used $H\alpha$ line widths to estimate velocity dispersion after correcting for the instrumental resolution. The velocity dispersions were calculated by $\sigma = \text{FWHM}/2.355 \times \frac{c}{\lambda}$, where the FWHM is the full width at half maximum in wavelength after subtraction of the instrumental resolution ($14 - 15 \text{ \AA}$ in the K -band) in quadrature. The velocity dispersions we measured were $131 \pm 5 \text{ km s}^{-1}$ and $112 \pm 4 \text{ km s}^{-1}$ for the apertures of SDSS J0901+1814, $69 \pm 4 \text{ km s}^{-1}$ and $58 \pm 3 \text{ km s}^{-1}$ for the apertures of the Cosmic Horseshoe, and $71 \pm 8 \text{ km s}^{-1}$, $73 \pm 6 \text{ km s}^{-1}$, and $80 \pm 4 \text{ km s}^{-1}$ for the two apertures and the full aperture of the Clone. Uncertainties in velocity dispersion were estimated using the same Monte Carlo approach that was applied to line fluxes.

3.3. Dust Extinction

It is important to understand the effects of dust extinction on the various line fluxes, as reddening by dust is highly wavelength dependent and thus can alter the observed flux ratios of widely spaced emission lines from their intrinsic values. Extinction in $z \geq 2$

TABLE 2
 EMISSION LINE FLUXES^a

	SDSS J0901+1814	SDSS J0901+1814	Cosmic Horseshoe	Cosmic Horseshoe	Clone	Clone	Clone
Aperture	1	2	1	2	1	2	Full
$\sigma_{\text{H}\alpha}^b$	131 ± 5	112 ± 4	69 ± 4	58 ± 3	71 ± 8	73 ± 6	80 ± 4
$F_{[\text{OII}]}$	< 9.0	< 10.0	18.8 ± 0.9	20.0 ± 1.0	29.0 ± 3.0	47.0 ± 3.0	85.0 ± 5.0
$F_{[\text{NeIII}]\lambda 3869}$	< 8.0	19.0 ± 3.0	< 4.0	< 4.0	< 17.0	< 16.0	< 28.0
$F_{[\text{H}\gamma]}$	-	-	3.0 ± 1.0	4.6 ± 0.4	6.0 ± 2.0	11.2 ± 0.7	21.0 ± 1.0
$F_{[\text{OIII}]\lambda 4363}$	-	-	< 1.5	< 1.6	< 2.6	< 2.4	< 4.3
$F_{\text{H}\beta}$	5.0 ± 2.0	$> 4^c$	8.0 ± 1.0	7.0 ± 1.0	15.0 ± 2.0	25.0 ± 2.0	33.0 ± 4.0
$F_{\text{H}\beta, \text{inf}}^d$	-	-	12.6 ± 0.3	16.2 ± 0.3	15.4 ± 0.6	36.0 ± 1.0	53.0 ± 1.2
$F_{[\text{OIII}]\lambda 4959}$	8.0 ± 2.0	11.0 ± 2.0	7.5 ± 0.8	9.6 ± 0.5	20.0 ± 1.0	35.0 ± 1.0	58.0 ± 2.0
$F_{[\text{OIII}]\lambda 5007}$	18.0 ± 4.0	39.0 ± 3.0	21.9 ± 0.6	31.2 ± 0.6	56.0 ± 1.0	106.0 ± 1.0	173.0 ± 2.0
$F_{\text{H}\alpha}$	63.0 ± 2.0	72.0 ± 1.0	43.4 ± 0.9	53.9 ± 0.9	61.0 ± 2.0	132.0 ± 4.0	202.0 ± 5.0
$F_{[\text{NII}]\lambda 6584}$	42.0 ± 1.0	64.0 ± 1.0	4.0 ± 0.7	8.7 ± 0.7	10.8 ± 0.9	21.0 ± 1.0	39.0 ± 2.0
$F_{[\text{SII}]\lambda 6717}$	12.0 ± 1.0^e	11.0 ± 1.0	$6.0 \pm 2.0^{e,g}$	4.0 ± 1.0^g	5.5 ± 0.9	10.0 ± 1.0	9.0 ± 2.0
$F_{[\text{SII}]\lambda 6732}$	12.0 ± 1.0^e	$> 6.4^f$	$6.0 \pm 2.0^{e,g}$	6.0 ± 1.0^g	7.3 ± 0.9	10.0 ± 1.0	12.0 ± 3.0

^a Emission line flux and error in units of 10^{-17} ergs s^{-1} cm^{-2}

^b One-dimensional $\text{H}\alpha$ velocity dispersion and error in units of km s^{-1} .

^c A sky line coincided with $\text{H}\beta$ for aperture 2 of SDSS J0901+1814, and the line flux value was found by summing only the positive flux, instead of fitting the line with a Gaussian.

^d These inferred $\text{H}\beta$ values are calculated from the observed broadband $g - r$ color and the value for $\text{H}\alpha$, as described in §3.3.

^e This value corresponds to the sum of the flux across both lines, with error.

^f A sky line coincided with $[\text{SII}]\lambda 6732$ for SDSS J0901+1814, aperture 2, and the line flux value was found by summing only the positive flux, instead of fitting the line with a Gaussian.

^g The spectra from apertures 1 and 2 were summed for the Cosmic Horseshoe in order to better measure the $[\text{SII}]$ line fluxes. The measured values were $F_{[\text{SII}]\lambda 6717} = 8 \pm 2$, and $F_{[\text{SII}]\lambda 6732} = 8 \pm 2$.

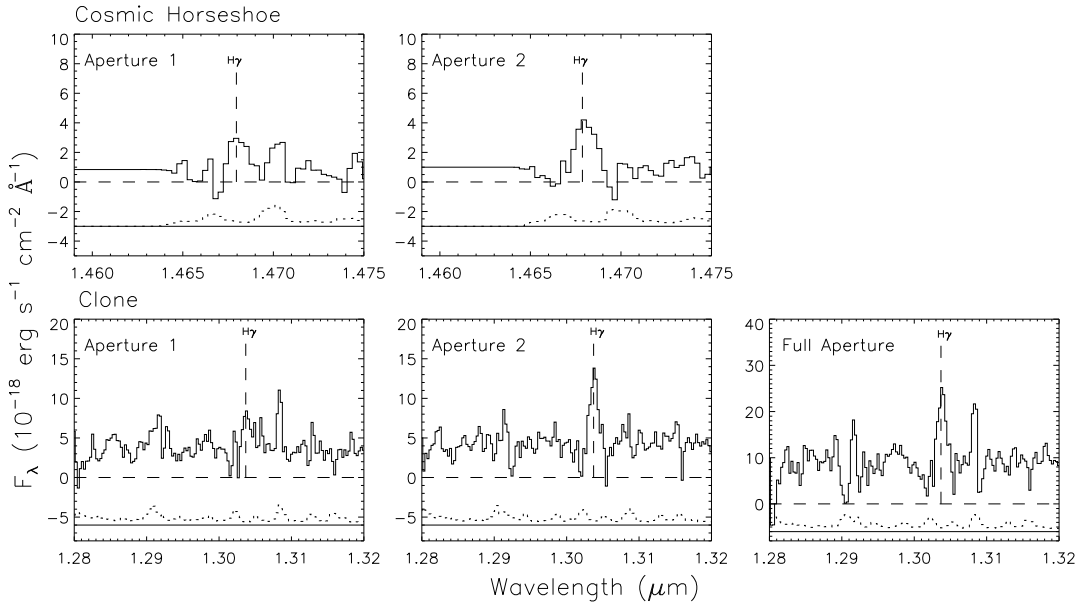


FIG. 6.— NIRSPEC spectra of the $\text{H}\gamma$ lines for the target objects. The dotted lower spectra indicate the 1σ errors offset vertically by -5×10^{-18} erg s^{-1} cm^{-2} \AA^{-1} for clarity.

star-forming galaxies is commonly estimated from rest-frame UV colors and an application of the Calzetti et al. (2000) starburst attenuation law. The Calzetti law appears to provide a fairly accurate description on average of the reddening and attenuation of the UV stellar continuum in both nearby and distant starburst galaxies (Reddy & Steidel 2004; Reddy et al. 2006). The degree of dust extinction in star-forming regions can also be estimated from the Balmer lines of hydrogen, because these strong optical lines have intrinsic ratios that are well described by atomic theory. Under the assumption of Case B recombination (Osterbrock 1989) and for

$T = 10,000$ K, the Balmer ratios are set. Any deviations in the observed line ratios are then attributed to dust extinction. Calzetti (2001) demonstrates that, in local star-forming galaxies, the stellar continuum suffers less reddening than the ionized gas, expressed as $E(B - V)_{\text{star}} = 0.44E(B - V)_{\text{gas}}$. Furthermore, Calzetti (2001) suggests that the reddening of the Balmer lines in nearby UV-selected starbursts is better described by a foreground dust distribution and traditional Milky Way extinction curve (Cardelli et al. 1989). On the other hand, Erb et al. (2006b) present evidence that, in $z \sim 2$ star-forming galaxies, $E(B - V)_{\text{star}} \simeq E(B - V)_{\text{gas}}$ and

a Calzetti et al. starburst extinction law applied to both UV-continuum and H α emission lines gives rise to the best agreement between UV- and H α -derived SFRs. Our new observations of the Cosmic Horseshoe and the Clone allow for a detailed comparison of different estimates of extinction in high-redshift star-forming galaxies.

First, we used the observed broadband $g - r$ color for our objects and an assumed intrinsic SED to obtain an estimate of $E(B - V)$. The SED model assumed was a Bruzual & Charlot (2003) solar metallicity, constant SFR model with stellar age of 570 Myr, as Erb et al. (2006c) find a median age of 570 Myr for star forming regions of galaxies at $z \sim 2$. We used SDSS g and r magnitudes for the Cosmic Horseshoe, and in the case of the Clone, the Apache Point Observatory SPICAM g and r magnitudes of the individual apertures presented in Lin et al. (2008). The $E(B - V)$ values we calculated were 0.16, 0.13 for the Cosmic Horseshoe, and 0.28, 0.21, and 0.24 for the Clone.

Next, extinction was estimated based on rest-frame optical emission lines. In both the Cosmic Horseshoe and the Clone, we have detected three of the most prominent Balmer lines: H α , H β , and (because of the magnification afforded by gravitational lensing) H γ . Unfortunately, in both objects, H β lines lay over prominent sky lines with systematically negative residuals, yielding in some cases unphysically low values of H β /H γ . Osterbrock (1989) gives the value of H β /H γ under Case B recombination as 2.14. Because reddening will only serve to increase this ratio, our measured values of less than 2.14 in aperture 2 of the Horseshoe and the full aperture of the Clone suggest that, in general, our measured H β values were systematically low as a result of the residual error in subtraction of the coincident sky line. H γ does not appear to suffer from the same systematic sky residuals as H β , and therefore we used a comparison of the observed and intrinsic ratios of H α /H γ to infer $E(B - V)_{\text{gas}}$, assuming an intrinsic H α /H γ ratio of 6.12 (Osterbrock 1989). To increase the S/N of the H γ feature, we combine spectra from individual apertures of each object to obtain an average H α /H γ and $E(B - V)_{\text{gas}}$. The observed H α /H γ ratios imply values of $E(B - V)_{\text{gas}}$ of 0.45 ± 0.04 and 0.28 ± 0.04 for the Cosmic Horseshoe and the Clone, respectively.

The value of $E(B - V)_{\text{gas}}$ for the Cosmic Horseshoe is almost three times higher than that inferred from the rest-frame UV continuum. While this difference at first appears to support the prescription from Calzetti et al. (2000), regarding the relative extinction of starlight and ionized gas, we argue in section 3.4 that the $g - r$ -based estimate of $E(B - V)$ provides a more robust estimate of the ionized gas extinction. In contrast, both $g - r$ and H α /H γ provide consistent estimates of dust extinction in the Clone, i.e., $E(B - V)_{\text{star}} \simeq E(B - V)_{\text{gas}}$. It is also worth noting that, over the wavelength range probed by our NIRSPEC spectra, the Calzetti et al. (2000) and Cardelli et al. (1989) extinction curves yield very similar values for $E(B - V)_{\text{gas}}$, as well as extinction-corrected line ratios. In all subsequent discussion, we adopt the Calzetti et al. (2000) extinction law and $E(B - V)$ values based on rest-frame UV colors.

One important application of our derived $E(B - V)$ values is for inferring H β fluxes, independent of sky residuals. We follow a similar methodology to that

of Lemoine-Busserolle et al. (2003), and calculate the H β flux based on the observed H α flux, the intrinsic ratio of 2.86 between H α and H β , and our estimated $E(B - V)$ based on $g - r$ colors. Accordingly, $F_{\text{H}\beta} = F_{\text{H}\alpha} / 2.86 \times 10^{-0.4E(B-V)(\kappa_{\beta} - \kappa_{\alpha})}$. In this expression, κ_{β} and κ_{α} refer to the extinction coefficients in the Calzetti et al. curve at the wavelengths of H β and H α , respectively. Inferred H β fluxes are listed in Table 2 and used in the calculation of physical quantities in subsequent sections.

3.4. Star-Formation Rate

SFRs were calculated from H α luminosities based on the calibrations of Kennicutt (1998), but including a normalization factor of 1.8 to convert from a Salpeter (1955) initial mass function (used by Kennicutt) to a Chabrier (2003) initial mass function. Lensing serves to increase the measured H α luminosity, and thus the SFR, by the magnification factor of the lensed image. In order to correct for lensing, we used the published lensing solutions for the Cosmic Horseshoe (Dye et al. 2008; Belokurov et al. 2007) and the Clone (Lin et al. 2008). The published magnification factors apply to the entirety of the Einstein ring and not to the individual knots that we targeted on our NIRSPEC apertures. We therefore used the VLT R and SDSS r -band images to find the fraction of the flux in the total Einstein ring that fell onto the slit (0.11 for the Cosmic Horseshoe and 0.30 for the Clone). Under the assumption that the rest-frame UV flux in these bands is proportional to the flux in H α , we divided the measured H α luminosity (for both apertures) by the fraction of flux that fell into the slit versus the total flux in the ring. This calculation yielded the H α luminosity for the entirety of the ring, which we could then convert to a lensed SFR and divide by the magnification to find the unlensed SFR. For the Cosmic Horseshoe, the magnification factor for the lens is 24 ± 2 (Dye et al. 2008), and adopting this lensing model, we calculated an unlensed SFR of $73 M_{\odot} \text{ yr}^{-1}$ without correcting for reddening, $113 M_{\odot} \text{ yr}^{-1}$ with the broadband $g - r$ color reddening correction and $289 M_{\odot} \text{ yr}^{-1}$ for the H α /H γ reddening correction. For the Clone, the magnification factor given for the lens is 27 ± 1 (Lin et al. 2008), and under this assumption, the unlensed SFR was $32 M_{\odot} \text{ yr}^{-1}$ without correcting for reddening, $64 M_{\odot} \text{ yr}^{-1}$ with the broadband $g - r$ color reddening correction and $75 M_{\odot} \text{ yr}^{-1}$ with the H α /H γ reddening correction. Based on the quoted uncertainties in the magnification factors and $E(B - V)$ values, the formal errors on the lensing- and dust-corrected SFRs are $\sim 15\%$, yet these errors do not fully reflect hard-to-quantify uncertainties in the fraction of the H α flux that fell into our slit and the underlying stellar absorption affecting the Balmer lines, and systematics in the lensing models.

SFRs can also be estimated from rest-frame UV luminosities, according to the relation presented in Kennicutt (1998). We use the optical photometry from Belokurov et al. (2007) and Lin et al. (2008) to obtain such estimates for the Cosmic Horseshoe and the Clone, respectively, again converting from a Salpeter to Chabrier IMF. We calculate an extinction-corrected $SFR_{\text{UV}} = 65 - 80 M_{\odot} \text{ yr}^{-1}$ for the Cosmic Horseshoe, where the range reflects the uncertainty in inferred $E(B - V)$ values ($\sim 0.13 - 0.16$, see Table 3) and magnification

TABLE 3
 CALCULATED PHYSICAL VALUES

	Cosmic Horseshoe	Cosmic Horseshoe	Clone	Clone	Clone
	1	2	1	2	Full
Aperture					
R_{23}	3.82 ± 0.13	3.78 ± 0.11	6.88 ± 0.35	5.25 ± 0.18	5.97 ± 0.18
R_{23}^a	4.08 ± 0.15	3.95 ± 0.12	7.45 ± 0.40	5.52 ± 0.20	6.36 ± 0.20
$N2$	-1.04 ± 0.07	-0.79 ± 0.04	-0.75 ± 0.04	-0.79 ± 0.02	-0.72 ± 0.02
$O3N2$	1.28 ± 0.08	1.08 ± 0.04	1.31 ± 0.05	1.26 ± 0.03	1.23 ± 0.02
$12 + \log(O/H)_{R_{23}}$	8.85 ± 0.05	8.85 ± 0.05	8.55 ± 0.05	8.70 ± 0.05	8.63 ± 0.05
$12 + \log(O/H)_{R_{23}}^a$	8.82 ± 0.05	8.84 ± 0.05	8.50 ± 0.05	8.68 ± 0.05	8.60 ± 0.05
$12 + \log(O/H)_{N2}$	8.31 ± 0.18	8.45 ± 0.18	8.47 ± 0.18	8.45 ± 0.18	8.50 ± 0.18
$12 + \log(O/H)_{O3N2}$	8.32 ± 0.14	8.38 ± 0.14	8.31 ± 0.14	8.33 ± 0.14	8.34 ± 0.14
O_{32}	1.56 ± 0.09	2.00 ± 0.12	2.61 ± 0.26	2.98 ± 0.20	2.73 ± 0.17
O_{32}^a	1.28 ± 0.07	1.70 ± 0.10	1.84 ± 0.18	2.28 ± 0.15	2.01 ± 0.12
$F_{[SII]\lambda 6717} / F_{[SII]\lambda 6734}$	-	0.7 ± 0.2	0.8 ± 0.1	1.0 ± 0.1	0.7 ± 0.1
$L_{H\alpha}^c$	17	17	7	7	7
$L_{H\alpha}^{a,c}$	26	26	15	15	15
$L_{H\alpha}^{b,c}$	66	66	17	17	17
$SFR_{H\alpha}^d$	73	73	32	32	32
$SFR_{H\alpha}^{a,d}$	113	113	64	64	64
$SFR_{H\alpha}^{b,d}$	289	289	75	75	75
$E(B - V)_{g-r}$	0.16	0.13	0.28^e	0.21^e	$0.24^{e,f}$
$E(B - V)_{H\alpha/H\gamma}$	0.45	0.45	0.28	0.28	0.28

^a These values are corrected for reddening by the broadband $g - r$ derived $E(B - V)$ values

^b These values are corrected for reddening by $E(B - V)$ values derived from $H\alpha/H\gamma$ values and assuming Case B recombination

^c $H\alpha$ luminosity in units of 10^{42} ergs s^{-1} , corrected for gravitational lensing, and summed across both apertures

^d SFR in units of $M_{\odot} \text{ yr}^{-1}$, corrected for gravitational lensing and summed across both apertures

^e g and r magnitudes taken from Lin et al. (2008)

^f g and r magnitudes for the full aperture of the Clone are taken from the flux of the individual apertures

cation factor. The UV-derived SFR is significantly lower than the SFR based on $H\alpha$ if the $H\alpha$ extinction correction is calculated from $H\alpha/H\gamma$. Much better agreement is found when the $E(B - V)$ value used to correct $H\alpha$ is based on the $g - r$ color. We therefore conclude that, in the case of the Cosmic Horseshoe, the $g - r$ color is a more reliable tracer of the extinction of both stars and gas than the $H\alpha/H\gamma$ ratio. For the Clone, we find an extinction-corrected $SFR_{UV} = 60 - 110 M_{\odot} \text{ yr}^{-1}$, corresponding to $E(B - V)$ values of $\sim 0.21 - 0.28$. This UV-derived SFR agrees very well with the extinction-corrected $H\alpha$ SFR (regardless of whether $g - r$ or $H\alpha/H\gamma$ is used to extinction-correct $H\alpha$). In conclusion, we present the extinction properties of the Cosmic Horseshoe and the Clone, along with a comparison of their $H\alpha$ and UV SFRs. These results support the findings of Erb et al. (2006b), that $E(B - V)_{\text{star}} \simeq E(B - V)_{\text{gas}}$ in $z \sim 2$ star-forming galaxies.

3.5. Metallicity

Our NIRSPEC measurements include a large number of rest-frame optical emission line fluxes, enabling the calculation of gas-phase metallicities for our objects. The gas-phase metallicity reflects the integrated products of previous star formation, modulated by gas inflow and outflow. Typically, oxygen is used to probe gas metallicity in star-forming galaxies as it is the most abundant heavy element, and is promptly released into the interstellar medium following a burst of star formation. Furthermore, the emission lines from the various ionization states of oxygen are strong and easily measurable in the rest-frame optical. In this paper, solar abundance is defined as $12 + \log(O/H) = 8.66$ (Allende Prieto et al. 2002; Asplund et al. 2004).

For local galaxies, the oxygen abundance can be in-

ferred from the electron temperature by comparing auroral lines (such as $[O \text{ III}]\lambda 4363$) to nebular emission lines (e.g. $[O \text{ III}]\lambda\lambda 4959, 5007$). Weak auroral lines are difficult to measure in high-redshift galaxies, where the ratios of various strong emission lines are used as a proxy for metallicity. These ratios have been calibrated as oxygen abundance indicators in local H II regions. The magnification from the strong-lensing has made it possible to obtain a large set of high quality measurements of emission lines in relatively short exposure times. We therefore can compare three strong-line ratios as oxygen abundance indicators: $R_{23} \equiv ([O \text{ II}]\lambda 3727 + [O \text{ III}]\lambda\lambda 4959, 5007/H\beta)$, $N2 \equiv \log\{([N \text{ II}]/H\alpha)\}$, and $O3N2 \equiv \log\{([O \text{ III}]\lambda 5007/H\beta) / ([N \text{ II}]\lambda 6584/H\alpha)\}$. $N2$ and $O3N2$ have been calibrated using direct O/H measurements for local H II regions by Pettini & Pagel (2004), and we used the R_{23} calibration from Tremonti et al. (2004), which has been calibrated with photoionization models. The observed strong-line ratios and inferred metallicities are listed in Table 3.

The R_{23} indicator was introduced by Pagel et al. (1979), and is widely used for measuring local metal abundances if the fluxes of $[O \text{ III}]$ and $[O \text{ II}]$ are known. Tremonti et al. (2004) provided an analytical fit to the R_{23} - metallicity relation for a set of local SDSS galaxies:

$$12 + \log(O/H) = 9.185 - 0.313x - 0.264x^2 - 0.321x^3 \quad (1)$$

where $x = \log R_{23}$. Since R_{23} is double valued for the larger values of the ratio, this formula is only valid for the high metallicity branch of the R_{23} -abundance relation. This relationship has a 1σ scatter of 0.05 dex for the sample of star-forming galaxies presented in Tremonti et al. (2004), though this error may underestimate the true systematic uncertainty (Kennicutt et al. 2003). For R_{23} ,

we used the values for the $H\beta$ flux that we inferred from the broadband color-derived value of $E(B - V)$. R_{23} is sensitive to reddening because of the large wavelength difference between $[O\ III]\lambda 5007$ and $[O\ II]\lambda 3727$. The observed [and extinction corrected] R_{23} values that we calculated for our objects were 3.82[4.07], 3.79[3.96] for the two apertures of the Cosmic Horseshoe, and 6.86[7.41], 5.25[5.52], and 5.93[6.32] for the two apertures and the full aperture of the Clone. The R_{23} values for apertures 1 and 2 of the Cosmic Horseshoe correspond to metallicities of $12 + \log(O/H) = 8.85[8.82]$ and $8.85[8.84]$, respectively. These are high relative to solar metallicity. For the Clone, the inferred metallicities for apertures 1, 2 and the full aperture are $12 + \log(O/H) = 8.55[8.50]$, $8.70[8.68]$, and $8.64[8.60]$, respectively. These values range from slightly subsolar to solar.

The $N2$ indicator is related to the oxygen abundance by:

$$12 + \log(O/H) = 8.90 + 0.57 \times N2 \quad (2)$$

which is valid for $7.50 < 12 + \log(O/H) < 8.75$. The relationship has a 1σ scatter of ± 0.18 dex on the y-intercept (Pettini & Pagel 2004). We found values of $N2 = -1.04$ and -0.79 ($12 + \log(O/H) = 8.31$ and 8.45) for the Cosmic Horseshoe, and -0.75 , -0.79 , and -0.72 ($12 + \log(O/H) = 8.47$, 8.45 , and 8.50) for the Clone. These values all indicate a subsolar gas metallicity.

We also measured values of the $O3N2$ indicator for our objects. This indicator is related to oxygen abundance by:

$$12 + \log(O/H) = 8.73 - 0.32 \times O3N2 \quad (3)$$

which is valid for $8.12 < 12 + \log(O/H) < 9.05$, with a 1σ scatter of ± 0.14 dex (Pettini & Pagel 2004). The errors shown for our oxygen abundances are dominated by the systematic uncertainties from the calibration, as opposed to measurement errors. For $O3N2$, we used the values of $H\beta$ that were calculated from the $g - r$ color, as described in §3.3. The values that we calculated are 1.28, 1.08 ($12 + \log(O/H) = 8.32$ and 8.38) for the Cosmic Horseshoe, and 1.31, 1.26, and 1.23 ($12 + \log(O/H) = 8.31$, 8.33 , and 8.34) for the Clone. These values indicate subsolar metallicities in the gas. The $N2$ and $O3N2$ indicators do not need to be dereddened due to the close spacing of the $[N\ II]$, $H\alpha$ lines and $[O\ III]$, $H\beta$ lines.

The $N2$ and $O3N2$ indicators yield consistent metallicities of ~ 0.5 solar for both the Cosmic Horseshoe and the Clone. However, the R_{23} indicator points to a significantly higher, and supersolar, metallicity in the Cosmic Horseshoe. Such systematic discrepancies between R_{23} and other indicators are well known among local star-forming galaxies, and reflect the current limitations of strong-line abundance indicators (Kewley & Ellison 2008; Kennicutt et al. 2003). For the Clone, R_{23} indicates a metallicity that is only slightly higher than, and statistically consistent with, the values implied by $N2$ and $O3N2$. As we will discuss in §4.2, the differences in metallicity for the Cosmic Horseshoe and the Clone based on R_{23} may reflect the relative positions of these objects with respect to the emission-line excitation sequence of local objects.

3.6. Ionization Parameter

The local ionization state in an H II region is often characterized by the ionization parameter, U , which is the ratio between the density of ionizing photons and the density of hydrogen atoms. Commonly, ionization parameters are estimated using $O_{32} = ([O\ III]\lambda\lambda 4959, 5007 / [O\ II]\lambda\lambda 3726, 3729)$, and corrected for reddening. We estimate extinction based on the observed $g - r$ colors. Our values of O_{32} , both uncorrected [and corrected] for extinction, are 1.56[1.28], 2.00[1.70] for the two apertures of the Cosmic Horseshoe, and 2.61[1.84], 2.98[2.28], and 2.73[2.01] for the two apertures and the full aperture of the Clone. Lilly et al. (2003) showed that a vast majority of local objects (from a Nearby Field Galaxy Survey B -selected local galaxy sample from Jansen et al. (2000)) have a value of $O_{32} < 1$, while the available data for objects at $z > 2$ (Pettini et al. 2001) indicate $O_{32} > 1$ (Pettini et al. 2001).

The value of O_{32} , however, is dependent not only on ionization parameter, but also, to a lesser extent, on metallicity (Kewley & Dopita 2002; Brinchmann et al. 2008). Kewley & Dopita (2002) provide formulae for relating observed values of O_{32} to ionization parameter, $\log(U)$, using photoionization models spanning a range of metallicities. We apply the relations for both 0.5 and $1.0Z_{\odot}$ models to translate our extinction-corrected O_{32} measurements into $\log(U)$ values. The adopted models reflect the range of metallicities inferred for the Cosmic Horseshoe and the Clone. At higher metallicities, a given value of O_{32} corresponds to a higher ionization parameter, so the $0.5Z_{\odot}$ models yield a lower bound to the inferred ionization parameters. Assuming $Z = 1.0Z_{\odot}$, we find $\log(U)$ ranging from -2.4 to -2.5 and -2.3 to -2.4 for the apertures of the Cosmic Horseshoe and the Clone, respectively. At $Z = 0.5Z_{\odot}$, the corresponding ionization parameters range from $\log(U) = -2.7$ to -2.8 and -2.5 to -2.6, i.e., 0.2 - 0.3 dex lower. The $\log(U)$ values inferred for 0.5 and $1.0Z_{\odot}$ models are very similar to the high ionization parameters (relative to local SDSS galaxies) inferred by Brinchmann et al. (2008) for the $z > 2$ objects in Pettini et al. (2001).

3.7. Electron Temperature and Density

The $[S\ II]\lambda\lambda 6717, 6732$ line ratio is sensitive to the electron density of an ionized gas. We used this line ratio in our objects to calculate the electron density for the ionized nebular gas. Similarly, the ratio ($[O\ III]\lambda\lambda 4959, 5007 / [O\ III]\lambda 4363$) is used to measure the electron temperature, as $[O\ III]$ has an energy-level structure that results in upper level emission lines with different excitation energies, whose relative strengths thus depend strongly on temperature. We used the IRAF procedure TEMDEN to calculate a range of densities and temperatures based on these line ratios.

Upper limits on the electron temperatures were measured from the $[O\ III]$ line ratios, since we were only able to measure upper limits for the $[O\ III]\lambda 4363$ line flux. For the lowest densities ($\sim 100\text{ cm}^{-3}$), the upper limits on the temperatures were 12,900 K and 12,200 K for the two apertures of the Cosmic Horseshoe and 13,200 K, 9,700 K and 10,000 K for the two apertures and the full aperture of the Clone, respectively. Changes in the density over the range 100 to 5000 cm^{-3} altered the calculated temperatures only very slightly.

We calculated densities from the measured $[S\ II]$ line

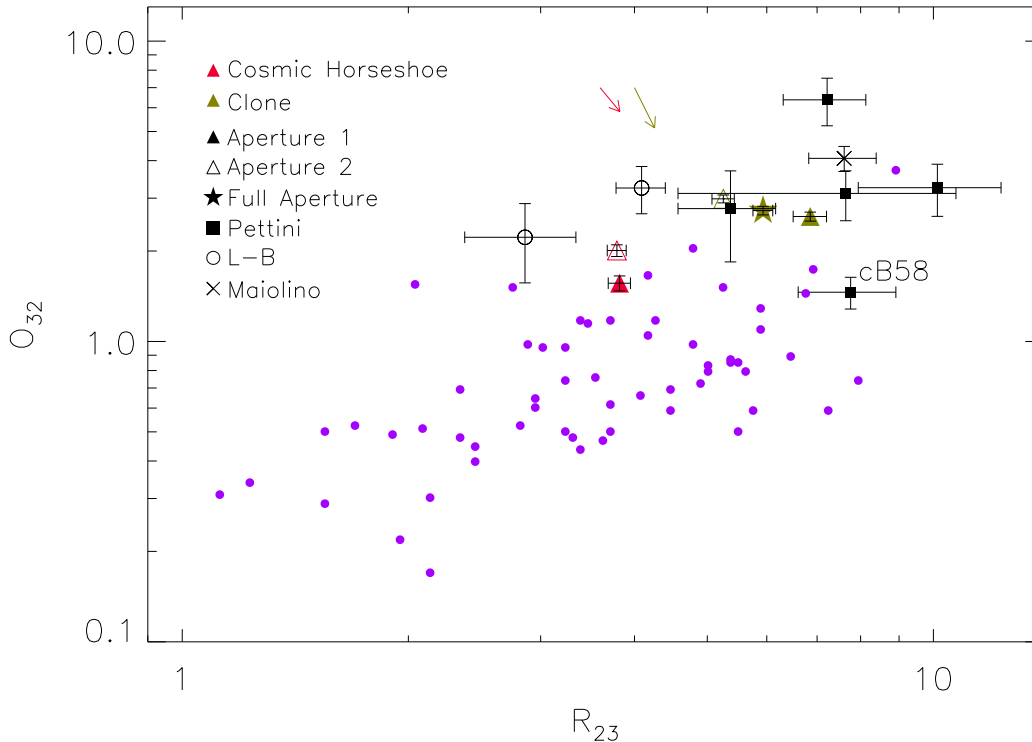


FIG. 7.— O_{32} versus R_{23} diagram. The apertures of the Cosmic Horseshoe and the Clone are plotted along with star-forming galaxies at intermediate and high redshift. A selection of $0.47 < z < 0.92$ objects from Lilly et al. (2003) are shown in purple. High-redshift points include five $z \sim 3$ LBGs from Pettini et al. (2001), two lensed $z \sim 1.9$ objects from Lemoine-Busserolle et al. (2003), and a composite spectrum of nine $z \sim 3.5$ LBGs from Maiolino et al. (2008). Symbols are described in the legend. The values on this plot are not corrected for dust extinction, however the red and green arrows indicate, respectively, the small impact of extinction corrections on the Cosmic Horseshoe and Clone data points. Such dust corrections will shift points downwards and to the right. The objects at $z \geq 2$ are systematically displaced on average with respect to the lower-redshift sample towards larger values of O_{32} , at fixed values of R_{23} . This empirical trend is evidence for higher ionization parameters at fixed metallicity (Kewley & Dopita 2002).

ratios in all apertures except for aperture 1 of the Cosmic Horseshoe, which had insufficient S/N. We also summed both apertures of the Cosmic Horseshoe to obtain an average, higher S/N, $[\text{S II}]$ line ratio estimate for the galaxy. In the calculation of densities we assumed a standard temperature of 10,000 K, consistent with our limits on electron temperatures. For each object the $\pm 1\sigma$ range in electron density was then derived from errors on the observed line ratios. For the Cosmic Horseshoe, Aperture 2, the $\pm 1\sigma$ range in electron density is $840 - 6900 \text{ cm}^{-3}$; for the summed Cosmic Horseshoe apertures, the corresponding range is $320 - 1600 \text{ cm}^{-3}$. For the Clone, apertures 1, 2, and full, we find ranges of $1110 - 2960 \text{ cm}^{-3}$, $530 - 1020 \text{ cm}^{-3}$, and $1270 - 2540 \text{ cm}^{-3}$. Despite the large uncertainties in the precise value of inferred electron density, the empirical fact remains that the high-redshift lensed targets exhibit systematically lower doublet ratios from what is typically observed in emission-line galaxies in the local universe (Liu et al. 2008).

4. ANALYSIS

4.1. Comparison to the $z \sim 2$ Population

Recent studies have been undertaken to understand the physical conditions of $z \sim 2$ objects (Erb et al. 2006a; Liu et al. 2008) and the observations presented here enable comparisons of the Cosmic Horseshoe and the Clone with the larger population of star-forming galaxies at

similar redshifts. The Cosmic Horseshoe and the Clone, based on their ugr colors, satisfy the criteria for UV-selected objects at $z \sim 2$ (Steidel et al. 2004). In the following analysis, we compare the physical quantities calculated from the rest frame optical line fluxes to those calculated in other high-redshift objects.

SFRs in high redshift objects have been measured in a variety of ways. We calculated lensing-corrected values for the SFR of $\sim 113 M_{\odot} \text{ yr}^{-1}$ based on our method of dereddening the $\text{H}\alpha$ fluxes for the Cosmic Horseshoe (i.e., from the $g - r$ color) and $64 - 75 M_{\odot} \text{ yr}^{-1}$ based on our method of dereddening for the Clone (i.e., from both the $g - r$ color and $\text{H}\alpha/\text{H}\gamma$ ratio). The average SFRs for a population of $z \sim 2$ galaxies from Erb et al. (2006b) is $\langle \text{SFR}_{\text{H}\alpha} \rangle = 31 \pm 18 M_{\odot} \text{ yr}^{-1}$. Our lensed targets are therefore more actively star-forming than average, but within the range spanned by the sample in Erb et al. (2006b). However, we caution that our calculated values depend on the magnification given by the particular lensing models that we used. For comparison, based on the $\text{H}\alpha$ flux and magnification factor of ~ 30 (Teplitz et al. 2000; Seitz et al. 1998) and with the assumption of a Chabrier initial mass function and Calzetti et al. (2000) dust extinction law with an estimated $E(B - V)_{\text{gas}} = 0.06$ (Siana et al. 2008), the SFR for MS1512-cB58 is $\text{SFR}(\text{H}\alpha) = 14 M_{\odot} \text{ yr}^{-1}$.

Erb et al. (2006c) measure an average velocity disper-

sion for a sample of $z \sim 2$ objects (with AGN removed) of $\langle \sigma \rangle = 108 \pm 5 \text{ km s}^{-1}$, and a standard deviation of 86 km s^{-1} . Our objects show a smaller velocity dispersion than the average, but are within the sample’s large standard deviation. While SDSS J0901+1814, in particular aperture 2, displays AGN-like line ratios, the velocity dispersions are very close to the average values for other $z \sim 2$ objects, indicating that SDSS J0901+1814 could be a narrow-line AGN. The dust extinction values that we infer from the $g-r$ color for the Cosmic Horseshoe are similar to the mean $E(B-V)$ value of 0.16 ± 0.01 from Erb et al. (2006c), while the Clone appears to be dustier than average, based on its $g-r$ color and $\text{H}\alpha/\text{H}\gamma$ ratio. Both objects are well within the range of extinction values spanned by $z \sim 2$ star-forming galaxies.

Our values for $N2$ ranged from -0.72 to -1.04 , within the interval spanned by the sample of $z \geq 2$ galaxies from Erb et al. (2006a). Values of R_{23} span from 4.0 to 7.4 , resulting in a range of metallicities that are slightly subsolar to slightly greater than solar, between $12+\log(\text{O}/\text{H}) = 8.5$ to 8.8 . Values for R_{23} from Pettini et al. (2001) for LBGs at $z \sim 3$ are within this range, between 4.0 and 12.3 , including a value of $R_{23} = 8.3$ for MS 1512-cB58. Lilly et al. (2003) plot star-forming galaxies at intermediate redshift ($0.47 < z < 0.92$) by their values for O_{32} versus R_{23} , and we reproduce their diagram in Figure 7, adding the Cosmic Horseshoe and Clone. To place our new observations in the context of other, similar measurements at high redshift, we also plot five LBGs at $z \sim 3$ from Pettini et al. (2001), two lensed objects at $z \sim 1.9$ from Lemoine-Busserolle et al. (2003), and the composite $z \sim 3.5$ spectrum from Maiolino et al. (2008), based on nine individual LBGs. In this plot, note that all of the values are as measured, and none have been dereddened. The effect of correcting the points for the Cosmic Horseshoe and Clone for dust extinction is indicated with reddening vectors. This diagram shows how objects at $z \geq 2$ have larger values of O_{32} (indicative of high values of the ionization parameter) for a given value of R_{23} (and thus, metallicity), relative to the sample from Lilly et al. (2003).

A common property of $z \geq 2$ star-forming galaxies is the kinematic evidence for star-formation feedback in the form of large-scale gas outflows (Pettini et al. 2001; Shapley et al. 2003). With measurements of the nebular, systemic redshifts for both the Cosmic Horseshoe and Clone, as well as rest-frame UV absorption-line spectra, it is possible to search for the signature of outflows. Using Keck II Echelle Spectrograph and Imager (ESI; Sheinis et al. 2002) rest-frame ultraviolet spectra of the Cosmic Horseshoe and the Clone, Quider et al. (2009) and Quider et al. (in preparation) analyze several of the strongest interstellar absorption features for kinematic evidence of large-scale gas outflow. In this analysis, redshifts measured for interstellar absorption lines were compared with those of $\text{H}\alpha$ and UV stellar photospheric features. For both targets, the slits were placed in the same position that was used for the NIRSPEC observations, and the spectra from the two apertures were summed to increase the signal-to-noise ratio. In the Cosmic Horseshoe, the average outflow velocity for the low-ionization interstellar absorption lines (e.g., Si II $\lambda 1260$, the O I + Si II $\lambda 1303$ doublet, Si II $\lambda 1527$, Al II $\lambda 1671$) is $\langle v_{out,low} \rangle = 146 \text{ km s}^{-1}$, and $\langle v_{out,high} \rangle = 167 \text{ km s}^{-1}$

for the high-ionization features (e.g., Si IV $\lambda\lambda 1394, 1403$, Al III $\lambda 1855$, Al III $\lambda 1863$). In the Clone, three low-ionization iron lines (Fe II $\lambda 2344$, 2383 , and 2600) were used to measure interstellar kinematics. These three lines indicate similar offsets, and the average outflow velocity is $\langle v_{out,low} \rangle = 154 \text{ km s}^{-1}$. The outflow velocities observed in the Cosmic Horseshoe and Clone are consistent with those calculated for star-forming galaxies at $z \sim 2$ (Steidel et al. 2004). Also, for comparison, the outflow velocity observed in MS 1512-cB58 is $\sim 255 \text{ km s}^{-1}$ (Pettini et al. 2002).

The $\text{H}\alpha$ velocity dispersion, σ , allows us to calculate the virial masses of our objects when combined with estimates of their sizes, using the half-light radius, $r_{1/2}$. We use the equation given by Pettini et al. (2001) for virial mass, assuming an idealized case of a sphere of uniform density:

$$M_{vir} = 1.2 \times 10^{10} M_{\odot} \frac{\sigma^2}{(100 \text{ km s}^{-1})^2} \frac{r_{1/2}}{\text{kpc}} \quad (4)$$

The lensing models for both the Cosmic Horseshoe and the Clone yield estimates of the intrinsic half-light radii, allowing us to calculate the virial masses of the objects.

The lensing model for the Cosmic Horseshoe (Dye et al. 2008) produces a source plane image with two objects, a “northern” and a “southern” source. These objects are lensed into ring-like distributions in the image plane, with slightly different morphologies. Accordingly, the relative contribution of the two sources varies as a function of position in the combined Einstein ring. The fainter, northern source, according to the Dye et al. (2008) model, contributes mostly to the portion of the Einstein ring that is not probed by our slit position, although the light from this source does contribute a small fraction of the emission in what we call aperture 1. The southern source, the more prominent of the two, is the only contributor to the emission in aperture 2 and constitutes the majority of the light in aperture 1. From the composite of the reconstructed source plane image, we estimated a half-light radius of the southern source of $\sim 0''.3$, which, at this redshift, and, for our adopted cosmology, corresponds to a size of $r_{1/2,CH} = 2.5 \text{ kpc}$. Thus, using the velocity dispersion for the second aperture, since it corresponds only to the southern source in the reconstructed image, we calculate a virial mass of the Cosmic Horseshoe of $M_{vir,CH} = 1.0 \times 10^{10} M_{\odot}$.

For the Clone, the lensing models described in Lin et al. (2008) and Allam et al. (2009, in preparation) yield estimates of the half-light radius in the reconstructed source plane of $\sim 0''.3$. At this redshift, the corresponding physical radius is $r_{1/2,Clone} = 2.9 \text{ kpc}$. The virial mass we calculated for the Clone, using the velocity dispersion from the full aperture, was $M_{vir,Clone} = 2.2 \times 10^{10} M_{\odot}$. Both the dynamical masses calculated for the Cosmic Horseshoe and the Clone are similar to the dynamical masses for objects at $z \sim 2$ from Erb et al. (2006c).

While the line flux ratios for the Clone are very similar between the apertures, the Dye et al. (2008) lensing model might help to explain the difference in the line flux ratios observed between the two apertures of the Cosmic Horseshoe. For instance, as seen in Table 2 and Figure 3, the [N II] and $\text{H}\alpha$ lines vary in strength with relation to

each other. One possible hypothesis concerns the level of contribution from the “northern” source to the first aperture of the lensed ring. If the gas in the fainter, northern source was at a lower metallicity, it would slightly lower the $[\text{N II}]/\text{H}\alpha$ line ratio of aperture 1 compared to aperture 2, which is what is observed in our data. Future analysis will be undertaken with the lensing model in order to disentangle the contribution from each object in the source plane.

In summary, we have shown that the SFRs, extinction values, metallicities, outflow velocities, and dynamical masses for our objects are relatively typical of those found among UV-selected star-forming galaxies at $z \sim 2$ (Steidel et al. 2004). We conclude that the Cosmic Horseshoe and the Clone are a representative sample of the luminous segment of the population of $z \sim 2$ objects. Future multi-wavelength observations of the broadband spectral energy distributions of the lensed targets will allow us to characterize their stellar masses and ages and therefore evolutionary states.

4.2. *The Offset in the $[\text{N II}]/\text{H}\alpha$ vs. $[\text{O III}]/\text{H}\beta$ diagram for High-Redshift Galaxies*

Recently, Shapley et al. (2005), Erb et al. (2006a), and Liu et al. (2008) have presented evidence indicating a difference between H II regions in high-redshift galaxies and those in local galaxies. The physical conditions in these regions are often probed by using the well known empirical diagnostic diagram of Baldwin, Phillips, & Terlevich (1981) (hereafter BPT). This diagram separates star-forming galaxies and AGN according to the optical line ratios $[\text{N II}]/\text{H}\alpha$ and $[\text{O III}]/\text{H}\beta$; star-forming galaxies fall in a region of lower $[\text{N II}]/\text{H}\alpha$ for a range of values of $[\text{O III}]/\text{H}\beta$. It has been demonstrated that a fraction of high redshift star-forming galaxies at $z \sim 1 - 2$ lie offset from the local population of H II regions and star-forming galaxies, displaced towards higher $[\text{N II}]/\text{H}\alpha$ and $[\text{O III}]/\text{H}\beta$ values. The strongly lensed, $z \sim 2$ objects are plotted on the BPT diagram in Figure 8 along with local emission-line objects from the fourth data release (DR4) of the SDSS (York et al. 2000; Adelman-McCarthy et al. 2006). The SDSS objects were selected to have $[\text{N II}]$, $\text{H}\alpha$, $[\text{O III}]$, and $\text{H}\beta$ line detections with $\text{S/N} > 5$. Also plotted on the diagram are curves designed to separate star forming galaxies and AGN; one line is from Kauffmann et al. (2003) that demarcates star-forming galaxies and AGN on an empirical basis, and the other from Kewley et al. (2001a) that represents a limit to the line-flux ratios that can be produced for star forming regions from photoionization plus stellar population synthesis models.

For both the Cosmic Horseshoe and the Clone, we plot two points for each aperture, one for each of method of calculating $\text{H}\beta$ fluxes. First, we plot upper limits on $[\text{O III}]/\text{H}\beta$ to reflect the fact that the measured $\text{H}\beta$ is a lower limit due to sky-subtraction residuals. Next, we plot circled symbols using the values of $\text{H}\beta$ flux inferred from $\text{H}\alpha$ and the $g - r$ color as described in §3.3. While SDSS J0901+1814 lies in the region occupied by local AGN, the two apertures of the Clone both appear in the area above the local star-forming regions. For the inferred $\text{H}\beta$ values, the line ratios for the Clone are shifted towards higher $[\text{O III}]/\text{H}\beta$ by 0.2 – 0.3 dex, relative to star-forming SDSS galaxies with similar $[\text{N II}]/\text{H}\alpha$ ra-

tios. Alternatively, the Clone is shifted towards higher $[\text{N II}]/\text{H}\alpha$ by 0.6 - 0.7 dex compared to SDSS galaxies with similar $[\text{O III}] / \text{H}\beta$ ratios. The interpretation is less straightforward for the Cosmic Horseshoe. Indeed, the $[\text{O III}]/\text{H}\beta$ upper limit for its second aperture is also offset from the local emission-line sequence, yet adopting the $\text{H}\beta$ value based on the $\text{H}\alpha$ flux and $g - r$ color places this aperture on the top edge of the locus of low-redshift galaxies. On the other hand, using the $\text{H}\alpha/\text{H}\gamma$ ratio to estimate the $\text{H}\beta$ flux results in an $[\text{O III}]/\text{H}\beta$ ratio that is midway between the two plotted symbols for this aperture, and, again, offset with respect to the local emission-line sequence. Our best estimate for aperture 2 of the Cosmic Horseshoe is that its point on the BPT diagram lies somewhere between top of the local emission-line sequence and the symbol indicating the upper limit for the aperture. In contrast, the point for aperture 1 of the Cosmic Horseshoe is consistent, or even below, the local emission-line sequence, depending on which value of $\text{H}\beta$ is adopted. Identifying the origin of the emission-line ratio variations within the Cosmic Horseshoe clearly requires a more detailed investigation, in concert with the lensing model for this system. Such analysis is outside the scope of the current work.

We have not corrected our $\text{H}\beta$ fluxes for possible stellar absorption at this wavelength. Stellar absorption would lead to an underestimate of the flux, and push the points upward on the BPT diagram. However, as noted in Shapley et al. (2005) and Erb et al. (2006a), the stellar $\text{H}\beta$ absorption line should have an equivalent width of only $W_{abs} \leq 5 \text{ \AA}$ (Charlot et al. 2002). Given that the Clone has $W_{H\beta} \geq 20 - 30 \text{ \AA}$, and the Cosmic Horseshoe does not have significant continuum detected in the spectral region near $\text{H}\beta$, stellar absorption is not significant. Furthermore, we defer application of this correction until the underlying stellar populations for the Cosmic Horseshoe and the Clone have been better constrained by deeper spectroscopy and multi-wavelength photometry.

While the Cosmic Horseshoe does not display the same clear offset as the Clone on the BPT diagram, when considered as a *population*, the sample of $z \sim 2$ objects with line ratio measurements (i.e., those presented in this paper as well as those in Erb et al. 2006a) appears to be offset on average from local galaxies. We have demonstrated that the Cosmic Horseshoe and Clone are typical of $z \sim 2$ star-forming galaxies in many respects, and also display several striking differences with respect to local galaxies in terms of their physical properties. As such, we will use the special insights afforded by gravitational lensing into the physical conditions in the Cosmic Horseshoe and Clone to explain the properties of the $z \sim 2$ population as a whole. We recognize the simplification associated with drawing conclusions based on only two objects, and the fact that a significantly larger sample of galaxies with the complete set of rest-frame optical emission lines is required to characterize the full $z \sim 2$ population. The discussion of the Cosmic Horseshoe and the Clone that follows represents the initial step in the direction of such a statistical study.

An important point of contrast between local star-forming galaxies in the SDSS and our high-redshift targets is the rate of star-formation activity. Shapley et al.

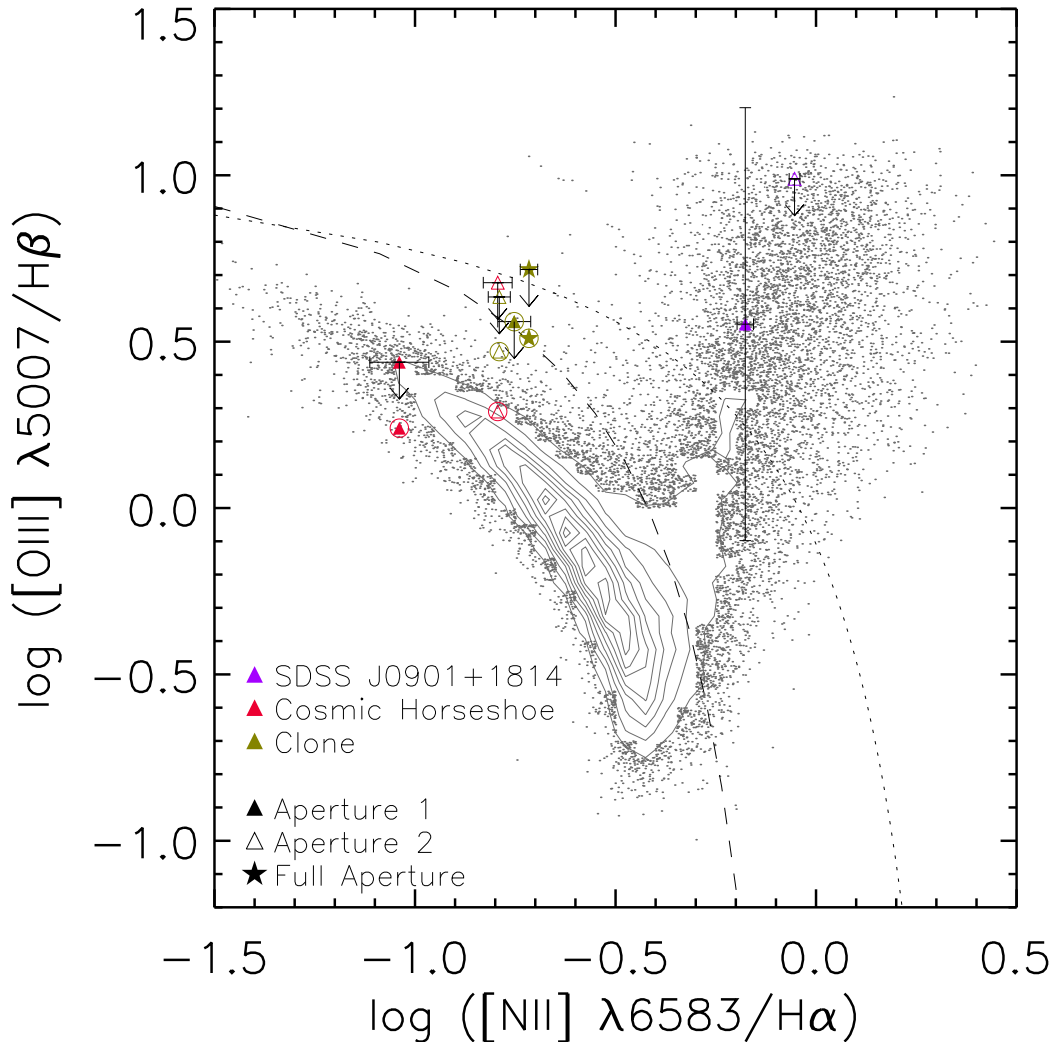


FIG. 8.— H II region diagnostic plot of $\log[\text{N II}]/\text{H}\alpha$ and $\log[\text{O III}]/\text{H}\beta$ emission line ratios. The grey points and contours represent SDSS local AGN and star forming galaxies that satisfy the criteria described in §4.2, while the lensed objects are as labeled in the legend. The circled objects are those where the $\text{H}\beta$ flux values were inferred from the $g-r$ color and $\text{H}\alpha$ fluxes. SDSS J0901+1814 points show large error bars due to the presence of a sky line on the $\text{H}\beta$ line in both apertures. The dashed line is an empirical demarcation between star-forming regions and AGN from Kauffmann et al. (2003) based on the SDSS galaxies, whereas the dotted line is the theoretical limit for star-forming galaxies from Kewley et al. (2001a). Local star-forming galaxies and H II regions exist in a well-defined excitation sequence due to photoionization by massive stars, and these are found to the left and below the curves. The apertures of the Clone, even with the inferred values of $\text{H}\beta$, are on average offset from this excitation sequence.

(2005) report an aperture-corrected mean SFR for a local sample of SDSS galaxies of $2.0 M_{\odot} \text{ yr}^{-1}$. These authors also noted that offset objects in the BPT diagram (both at high redshift and in the local SDSS sample) seem to exhibit elevated SFRs relative to the local average, and this is further demonstrated in a small sample of extreme SDSS galaxies in Liu et al. (2008). We estimate lensing-corrected SFRs in the Clone and Cosmic Horseshoe that are even higher than those presented in Shapley et al. (2005), more than an order of magnitude larger than the average SDSS SFR.

The higher rate of star formation might lead to a larger reservoir of ionizing photons, which is reflected in the ionization parameter. Brinchmann et al. (2008) demonstrated that the diagnostic line ratios in the BPT diagram are strongly dependent on the ionization param-

eter. However, while previous discussion of the offset has only provided possible explanations that could lead to this effect, our measurement of a host of lines, such as $[\text{O II}]\lambda\lambda 3726, 3729$ in the magnified objects, allows us to test this discussion more quantitatively. To date, only a small sample of ionization parameter measurements have been obtained for objects at $z \geq 2$ (Pettini et al. 2001; Lemoine-Busserolle et al. 2003; Maiolino et al. 2008). In both the Cosmic Horseshoe and the Clone, our measurements of O_{32} indicate higher values of the ionization parameter than seen in even the most extreme low- z UV selected galaxies from Contini et al. (2002), or a sample of star-forming galaxies at intermediate redshift ($0.47 < z < 0.92$) from Lilly et al. (2003). Figure 7 illustrates this point very clearly, in that, at fixed metallicity (i.e., R_{23}) high-redshift galaxies are offset on aver-

age towards significantly higher O_{32} (i.e., ionization parameter). If O_{32} values were considered in isolation, the differences in O_{32} between low- and high-redshift samples could simply be attributed to metallicity differences. However, the addition of R_{23} measurements indicates that there is a real effect towards systematically higher ionization parameters at high redshift.

Another idea discussed in Brinchmann et al. (2008) and Liu et al. (2008) is that the higher ionization parameter that might lead to this offset on the BPT diagram is due to a higher density in the H II regions. The [S II] $\lambda\lambda 6717, 6732$ line ratio allowed us to measure the density of the star forming regions in the Cosmic Horseshoe and the Clone, and the low resulting ratios indicated high densities of about $\sim 10^3 \text{ cm}^{-3}$, which is an order of magnitude higher than the values encountered in local starbursts (Kewley et al. 2001b). The ESI spectra analyzed by Quider et al. (2009) and Quider et al. (in preparation) also show another independent measure of the density in the form of the [C III] $\lambda 1907$ /[C III] $\lambda 1909$ line ratio. With this line ratio, values of about 1.5 and above are in the low density regime, while values from 0.2 and lower are in the high density regime. For the Cosmic Horseshoe, deblending the two lines in a smoothed spectrum yields a line ratio of 1.1 ± 0.2 , and for the Clone, the line ratio is 1.2 ± 0.2 . The values for the Cosmic Horseshoe and the Clone indicate densities ranging from $5000 - 22000 \text{ cm}^{-3}$ and $3000 - 17000 \text{ cm}^{-3}$, respectively. These are at least as high as those derived from the [S II] doublet (Osterbrock 1989). Brinchmann et al. (2008) calculate that densities of this order would account for an increase in the ionization parameter, which might lead to the observed offset on the BPT diagram.

5. CONCLUSIONS

We present NIRSPEC rest-frame optical spectra of three strongly-lensed $z \sim 2$ galaxies. These include SDSS J0901+1814 ($z = 2.26$), which, due to its observed line ratios, is possibly contaminated by an AGN; and two star-forming galaxies, the Cosmic Horseshoe ($z = 2.38$) and the Clone ($z = 2.00$). The general physical properties of the Cosmic Horseshoe and the Clone are representative of the properties found for star-forming galaxies at the same redshift. Specifically, we have measured the SFR from the $H\alpha$ luminosity, corrected for reddening and magnification from the lensing, and found it to be high yet typical of other measurements of high-redshift star formation (SFR = $\sim 110 M_{\odot} \text{ yr}^{-1}$ for the Cosmic Horseshoe and $\sim 70 M_{\odot} \text{ yr}^{-1}$ for the Clone). We have also used the R_{23} , $N2$, and $O3N2$ methods to calculate the metallicity of the H II regions, and found that, while there are differences among the metallicities calculated from these indicators, we can still constrain the metallicities to range from slightly sub-solar to solar. The dy-

namical masses calculated from $H\alpha$ velocity dispersions and the half-light radii of the reconstructed sources are on the order of $10^{10} M_{\odot}$, which is typical of the dynamical masses of UV-selected star-forming galaxies at $z \sim 2$. Finally, ESI rest-frame UV spectra provide evidence for the existence of outflowing gas with a velocity on the order of $\sim 150 - 200 \text{ km s}^{-1}$ for the Cosmic Horseshoe and the Clone, which are also similar to outflows seen in other high-redshift galaxies (Pettini et al. 2001; Steidel et al. 2004; Adelberger et al. 2003). In the future, it will be valuable to model the stellar populations of our lensed targets using multi-wavelength broadband photometry, and therefore obtain constraints on their stellar masses and ages.

The combination of strong lensing and NIRSPEC observations has allowed us to probe physical conditions that to date have been largely unexplored at $z \geq 2$. The measurements of the [S II] $\lambda\lambda 6717, 6732$ line ratio indicated high densities ($\sim 10^3 \text{ cm}^{-3}$) in these regions, in agreement with the densities derived from [C III] $\lambda 1907$ /[C III] $\lambda 1909$ line ratios for both objects. Large ionization parameters were measured by using O_{32} , which further indicates the high ionization state of the gas in high-redshift objects. The high values for the ionization parameter, density, and SFR in both the Cosmic Horseshoe and the Clone help in understanding why, on average, the population of high-redshift objects are offset on the BPT diagram, a standard diagnostic for star-forming regions (Shapley et al. 2005; Erb et al. 2006a; Liu et al. 2008). The exceptional data quality enables the measurement of quantities that previously were only speculation for $z \sim 2$ galaxies. These results offer more concrete evidence of the different conditions under which star formation occurs in galaxies at high redshift, yet a statistical sample is still required to place the results on firmer ground. Future observations with the Multi-Object Spectrometer for Infra-Red Exploration (MOSFIRE) instrument planned for the Keck I telescope will allow for the assembly of a much larger sample of rest-frame optical emission lines for this type of analysis.

We would like to thank Xin Liu, Anna Quider, Simon Dye, Thomas Diehl, and Huan Lin for their assistance. We acknowledge Lindsay King for kindly providing the VLT/FORS2 R -band image of the Cosmic Horseshoe. A.E.S. acknowledges support from the David and Lucile Packard Foundation and the Alfred P. Sloan Foundation. We wish to extend special thanks to those of Hawaiian ancestry on whose sacred mountain we are privileged to be guests. Without their generous hospitality, most of the observations presented herein would not have been possible.

REFERENCES

- Adelberger, K. L., Steidel, C. C., Shapley, A. E., & Pettini, M. 2003, *ApJ*, 584, 45
 Adelman-McCarthy et al. 2006, *ApJS*, 162, 38
 Allam, S. S., Tucker, D. L., Lin, H., Diehl, H. T., Annis, J., Buckley-Geer, E. J., & Frieman, J. A. 2007, *ApJ*, 662, L51
 Allende Prieto, C., Lambert, D. L., & Asplund, M. 2002, *ApJ*, 573, L137
 Asplund, M., Grevesse, N., Sauval, A. J., Allende Prieto, C., & Kiselman, D. 2004, *A&A*, 417, 751
 Baker, A. J., Lutz, D., Genzel, R., Tacconi, L. J., & Lehnert, M. D. 2001, *A&A*, 372, L37
 Belokurov, V., Evans, N. W., Moiseev, A., King, L. J., Hewett, P. C., Pettini, M., Wyrzykowski, L., McMahon, R. G., Smith, M. C., Gilmore, G., Sanchez, S. F., Udalski, A., Kozlov, S., Zucker, D. B., & Walcher, C. J. 2007, *ApJ*, 671, L9
 Bouwens, R. J., Illingworth, G. D., Franx, M., & Ford, H. 2007, *ApJ*, 670, 928
 Brinchmann, J., Pettini, M., & Charlot, S. 2008, *MNRAS*, 385, 769

- Bruzual, G. & Charlot, S. 2003, MNRAS, 344, 1000
- Calzetti, D. 2001, PASP, 113, 1449
- Calzetti, D., Armus, L., Bohlin, R. C., Kinney, A. L., Koornneef, J., & Storchi-Bergmann, T. 2000, ApJ, 533, 682
- Cardelli, J. A., Clayton, G. C., & Mathis, J. S. 1989, ApJ, 345, 245
- Chabrier, G. 2003, PASP, 115, 763
- Charlot, S., Kauffmann, G., Longhetti, M., Tresse, L., White, S. D. M., Maddox, S. J., & Fall, S. M. 2002, MNRAS, 330, 876
- Contini, T., Treyer, M. A., Sullivan, M., & Ellis, R. S. 2002, MNRAS, 330, 75
- Dye, S., Evans, N. W., Belokurov, V., Warren, S. J., & Hewett, P. 2008, MNRAS, 388, 384
- Erb, D. K., Shapley, A. E., Pettini, M., Steidel, C. C., Reddy, N. A., & Adelberger, K. L. 2006a, ApJ, 644, 813
- Erb, D. K., Shapley, A. E., Steidel, C. C., Pettini, M., Adelberger, K. L., Hunt, M. P., Moorwood, A. F. M., & Cuby, J. 2003, ApJ, 591, 101
- Erb, D. K., Steidel, C. C., Shapley, A. E., Pettini, M., Reddy, N. A., & Adelberger, K. L. 2006b, ApJ, 647, 128
- , 2006c, ApJ, 646, 107
- Jansen, R. A., Fabricant, D., Franx, M., & Caldwell, N. 2000, ApJS, 126, 331
- Kauffmann, G., Heckman, T. M., Tremonti, C., Brinchmann, J., Charlot, S., White, S. D. M., Ridgway, S. E., Brinkmann, J., Fukugita, M., Hall, P. B., Ivezić, Z., Richards, G. T., & Schneider, D. P. 2003, MNRAS, 346, 1055
- Kelson, D. D. 2003, PASP, 115, 688
- Kennicutt, R. C. 1998, ARA&A, 36, 189
- Kennicutt, R. C., Bresolin, F., & Garnett, D. R. 2003, ApJ, 591, 801
- Kewley, L. J. & Dopita, M. A. 2002, ApJS, 142, 35
- Kewley, L. J., Dopita, M. A., Sutherland, R. S., Heisler, C. A., & Trevena, J. 2001a, ApJ, 556, 121
- Kewley, L. J. & Ellison, S. L. 2008, ApJ, 681, 1183
- Kewley, L. J., Heisler, C. A., Dopita, M. A., & Lumsden, S. 2001b, ApJS, 132, 37
- Lemoine-Busserolle, M., Contini, T., Pelló, R., Le Borgne, J.-F., Kneib, J.-P., & Lidman, C. 2003, A&A, 397, 839
- Lilly, S. J., Carollo, C. M., & Stockton, A. N. 2003, ApJ, 597, 730
- Lin, H., Buckley-Geer, E., Allam, S. S., Tucker, D. L., Diehl, H. T., Kubik, D., Kubo, J. M., Annis, J., Frieman, J. A., Oguri, M., & Inada, N. 2008, ArXiv e-prints
- Liu, X., Shapley, A. E., Coil, A. L., Brinchmann, J., & Ma, C.-P. 2008, ApJ, 678, 758
- Madau, P., Ferguson, H. C., Dickinson, M. E., Giavalisco, M., Steidel, C. C., & Fruchter, A. 1996, MNRAS, 283, 1388
- Maiolino, R., Nagao, T., Grazian, A., Cocchia, F., Marconi, A., Mannucci, F., Cimatti, A., Pipino, A., Ballero, S., Calura, F., Chiappini, C., Fontana, A., Granato, G. L., Matteucci, F., Pastorini, G., Pentericci, L., Risaliti, G., Salvati, M., & Silva, L. 2008, A&A, 488, 463
- McLean, I. S., Becklin, E. E., Bendiksen, O., Brims, G., Canfield, J., Figer, D. F., Graham, J. R., Hare, J., Lacayanga, F., Larkin, J. E., Larson, S. B., Levenson, N., Magnone, N., Teplitz, H., & Wong, W. 1998, in Proc. SPIE Vol. 3354, p. 566-578, Infrared Astronomical Instrumentation, Albert M. Fowler; Ed., Vol. 3354, 566-578
- Osterbrock, D. E. 1989, Astrophysics of gaseous nebulae and active galactic nuclei (Research supported by the University of California, John Simon Guggenheim Memorial Foundation, University of Minnesota, et al. Mill Valley, CA, University Science Books, 1989, 422 p.)
- Pagel, B. E. J., Edmunds, M. G., Blackwell, D. E., Chun, M. S., & Smith, G. 1979, MNRAS, 189, 95
- Pettini, M. & Pagel, B. E. J. 2004, MNRAS, 348, L59
- Pettini, M., Rix, S. A., Steidel, C. C., Adelberger, K. L., Hunt, M. P., & Shapley, A. E. 2002, ApJ, 569, 742
- Pettini, M., Shapley, A. E., Steidel, C. C., Cuby, J., Dickinson, M., Moorwood, A. F. M., Adelberger, K. L., & Giavalisco, M. 2001, ApJ, 554, 981
- Pettini, M., Steidel, C. C., Adelberger, K. L., Dickinson, M., & Giavalisco, M. 2000, ApJ, 528, 96
- Quider, A. M., Pettini, M., Shapley, A. E., & Steidel, C. C. 2009, MNRAS, submitted.
- Reddy, N. A. & Steidel, C. C. 2004, ApJ, 603, L13
- Reddy, N. A., Steidel, C. C., Fadda, D., Yan, L., Pettini, M., Shapley, A. E., Erb, D. K., & Adelberger, K. L. 2006, ApJ, 644, 792
- Salpeter, E. E. 1955, ApJ, 121, 161
- Sawicki, M. 2001, AJ, 121, 2405
- Seitz, S., Saglia, R. P., Bender, R., Hopp, U., Belloni, P., & Ziegler, B. 1998, MNRAS, 298, 945
- Shapley, A. E., Steidel, C. C., Pettini, M., & Adelberger, K. L. 2003, ApJ, 588, 65
- Shapley, A. E., Coil, A. L., Ma, C.-P., & Bundy, K. 2005, ApJ, 635, 1006
- Sheinis, A. I., Bolte, M., Epps, H. W., Kibrick, R. I., Miller, J. S., Radovan, M. V., Bigelow, B. C., & Sutin, B. M. 2002, PASP, 114, 851
- Siana, B., Teplitz, H. I., Chary, R.-R., Colbert, J., & Frayer, D. T. 2008, ApJ, 689, 59
- Smail, I., Swinbank, A. M., Richard, J., Ebeling, H., Kneib, J.-P., Edge, A. C., Stark, D., Ellis, R. S., Dye, S., Smith, G. P., & Mullis, C. 2007, ApJ, 654, L33
- Steidel, C. C., Adelberger, K. L., Giavalisco, M., Dickinson, M., & Pettini, M. 1999, ApJ, 519, 1
- Steidel, C. C., Shapley, A. E., Pettini, M., Adelberger, K. L., Erb, D. K., Reddy, N. A., & Hunt, M. P. 2004, ApJ, 604, 534
- Teplitz, H. I., McLean, I. S., Becklin, E. E., Figer, D. F., Gilbert, A. M., Graham, J. R., Larkin, J. E., Levenson, N. A., & Wilcox, M. K. 2000, ApJ, 533, L65
- Tremonti, C. A., Heckman, T. M., Kauffmann, G., Brinchmann, J., Charlot, S., White, S. D. M., Seibert, M., Peng, E. W., Schlegel, D. J., Uomoto, A., Fukugita, M., & Brinkmann, J. 2004, ApJ, 613, 898
- Williams, L. L. R. & Lewis, G. F. 1996, MNRAS, 281, L35
- Yee, H. K. C., Ellingson, E., Bechtold, J., Carlberg, R. G., & Cuillandre, J.-C. 1996, AJ, 111, 1783
- York, D. G. et al. 2000, AJ, 120, 1579